Fluid Dynamic Mechanisms for the Wake Energy Recovery in Cross-Flow Turbines: Effects of Hydrofoil Shape and Turbine Solidity

MARINE 2021

Stefania Zanforlin[*] and Paola Lupi

Dipartimento di Ingegneria dell'Energia, dei Sistemi, del Territorio e delle Costruzioni (DESTEC)
Scuola di Inegneria, Università di Pisa
l.go Lazzarino 1, 56100 Pisa, Italy

[*] Corresponding author: Stefania Zanforlin, stefania.zanforlin@unipi.it

ABSTRACT

Cross-flow turbines (CFTs) are arousing a growing interest to harvest both off-shore wind and tidal currents. A promising characteristic of CFTs could be a high power-density in case of multi-device clusters or farms, achievable by shortening the distance between arrays as allowed by the fast energy recovery observed inside the wakes. However just few studies, only concerning symmetrical airfoils/hydrofoils, are found in literature. By means of 3d-URANS simulations and the momentum budget approach we investigated the effects of blade profile and turbine solidity on blade tip vortex generation and then on the mixing mechanisms supporting the reintroduction of streamwise momentum into the wake. Results indicate that: (a) a pair of counter-rotating vortices occurs in the wake at the turbine top and bottom ends, which rotation verse depends on blade profile and it is such as to generate positive vertical advection for camber-out profiles, but negative vertical advection for camber-in profiles; (b) camber-out profiles are much more effective in supporting the wake energy recovery due to the massive vertical advection induced by tip vortices; (c) for camber-in profiles the tip vortices poorly contribute to the wake recovery, that appears delayed and promoted by turbulent transport; (d) higher solidity implies stronger tip vortices and higher turbulent transport, therefore a faster wake recovery.

Keywords: tidal turbine; wake recovery; tip vortex; 3d URANS.

1. INTRODUCTION

Cross-flow turbines (CFTs) can be considered a valid alternative to horizontal axis turbines (HATs) to harvest the kinetic energies of off-shore wind and tidal currents, thanks to advantageous characteristics: simplicity and therefore low construction costs, ability to work independently of flow direction and, in case of a floating platform sustaining the rotor, more stability in off-shore wind applications, or the possibility of setting generator and gearbox above the sea level in tidal current applications. On the other hand, CFTs are penalized by low starting-torque and lower efficiency than HATs. However, the strong point of CFTs compared to HATs, which would more than compensate for the lower efficiency of the single device, is the higher power density achievable in case of a multi-device cluster or farm, i.e. the possibility of generating a greater amount of electrical energy from a sea limited area. To this end, the devices should be placed tightly by adopting pairs of closely-spaced counter-rotating turbines, that can exploit beneficial fluid dynamic interactions (Dabiri 2011; Zanforlin and Nishino 2016; Brownstein *et al.* 2019), or by shortening the distances between arrays, as allowed by the fast energy recovery experimentally measured for the first time by Kinzel *et al.* (2012) in the wakes of a CFT cluster. To plan efficient layouts for turbine farms, it is of crucial importance to know in depth the energy recovery mechanisms of the wake and to understand which operating and turbine geometrical parameters can support them but, at now, only few studies can be found in literature on this subject. The experimental investigations by Bachant and Wosnik (2015) and Rolin and Porté-Agel (2018) on the 3d-character of straight-bladed CFT wakes have shown that the vertical advection induced downstream the rotor by pairs of counter-rotating vortices occurring at the turbine top and bottom sides plays a dominant role in wake dynamics by entraining faster fluid from the freestream and therefore by supporting an extraordinary wake recovery that makes CFT wakes much shorter than HAT wakes. These vortex pairs are deemed the

consequence and evolution of the vortex shedding occurring at the blade tips, although they are visible even in case the blade tips are closed by plates, as observed by Ryan *et al.* (2016), who also tested the role of Tip Speed Ratio (*TSR=RΩ/U$_0$*, where *R* is the turbine radius, Ω is the angular speed, and *U$_0$* is the freestream velocity) finding that the strength of the vortex pair increases with *TSR*. To understand the energy recovery process of the wake in a more comprehensive way, it is possible to combine the direct observation of the main variables of the flow field (velocity and turbulence components) obtainable from experimentation or CFD with an analysis based on the momentum budget approach, which allows to quantify the role of advection and turbulent and viscous transport in the replenishment of the streamwise momentum deficit. In addition to Bachant and Wosnik (2015) and Rolin and Porté-Agel (2018), momentum budget analyses can be also found in the experimental study by Ouro *et al.* (2019) on a Gorlov-type CFT, and in the Large Eddy Simulation (LES) study by Posa (2020), despite this last study does not allow to consider vertical advection due to the 2.5d nature of the CFD simulations. Some common trends are observable in those studies: in the near-wake the dominant mechanisms are vertical (positive contribution) and lateral (negative contribution) advections whereas turbulent transport is much less and becomes important only in the medium-far wake. However, it should be noted that the aforementioned investigations are concerning symmetrical airfoils/hydrofoils (except for Ryan *et al.* 2016), and only high turbine solidities (*σ=Bc/πD*, where *B* is the blade number, *c* is the blade chord and *D* is the rotor diameter), typical of tidal current applications (*σ=14% in Bachant and Wosnik 2015, 17% in Rolin and Porté-Agel 2018, 32% in Ryan *et al.* 2016, and 21% in Ouro *et al.* 2019). Moreover, to our knowledge, there are no studies in which an attempt is made to make a quantitative comparison of the energy recovery between CFTs of different geometry. In our study we combine qualitative observations of the flow field achieved through 3d-URANS simulations with a momentum budget analysis to investigate the effects of blade profile and turbine solidity on blade tip vortex generation and then on the mixing mechanisms supporting the reintroduction of streamwise momentum into the wake. A hydrokinetic turbine with 3 straight blades, and operating at high Reynolds (typical of both tidal and large-scale wind turbines), is assumed. Two hydrofoils based on NACA0018 are considered: one is curved on the circumference describing the blade path (in the following, "camber-in"), the other one is specular to it ("camber-out"). Two turbine solidities, low and high, are chosen to represent wind and tidal applications, respectively.

2. METHODOLOGY

In this section the validation of the 3d numerical model is presented in comparison to experimental data available in literature about velocity profiles in the wake of a CFT. Next, the fundamentals of the momentum budget analysis are recalled, and the details of the methodology that we adopted to calculate the terms appearing in the equation are described.

2.1   Set-up and validation of the CFD model

ANSYS-ICEM has been used to generate multi-block structured 3d grids, with the addition of O-grids to thicken the distribution of cells in the areas of greatest interest and at the same time to improve their quality. Two grid levels are used to simulate the blade rotation via the sliding mesh method: a fixed sub-grid with the outer dimensions of the flow domain and a rotating sub-grid including the turbine blades. All around the blades the grid is very fine to make sure that *y+* at the walls stay below 0.4, following the work of Maître *et al.* (2013), who analysed the effect of *y+* realizing that averaged *y+>*1 causes a pressure drag overestimation in turbines exposed to significant flow separation, as happens for high solidity hydrokinetic turbines. The moving and the fixed domains are joined together by means of a boundary condition (BC) of interface. The other BC are: velocity inlet for the inlet face; pressure outlet for the exit; symmetry for the top boundary; wall for the bottom in case of the validation case study (since it corresponds to the wind tunnel floor) or symmetry for the main simulations of this paper (since only half turbine is simulated to save computation time).

The simulations are performed using ANSYS-Fluent v19. To model the turbulence, the k-ω SST (Shear Stress Transport) is adopted (Menter 1994; Wilcox 2008); this model is widely used in the simulation of wind and tidal CFTs since it is considered well appropriate in case of flow characterised by strong adverse pressure as happens in CFTs, especially when operating at low *TSR*. The algorithm for the velocity-pressure coupling is SIMPLEC. About the spatial discretization scheme, the Least Squares Cell-Based (LSCB) is set for gradient; pressure interpolation, turbulent kinetic energy and specific dissipation rate formulations are based on second order schemes. Temporal discretization is also based on a second order implicit method. The convergence

criteria for each time-step is 1×10^{-4} for the residuals of continuity, velocity components, turbulence kinetic energy and specific dissipation rate. When using a sliding mesh, to obtain a satisfactory numeric convergence the time-step should not be larger than the time required for advance the mobile interface by a distance corresponding to one cell thus, in order to consider the smallest cell at the interface, a time-step corresponding to $0.5°$ of revolution is adopted; this value is also in accordance with Balduzzi *et al.* (2016).

Since the current paper is focused on the wake dynamics, before to simulate the turbines of interest, the reliability of the overall numerical model has been verified by comparison with the wake experimental data of Vergaerde *et al.* (2020). We have chosen these data because of the very large test section of the wind tunnel, that avoid any blockage effect. The turbine has two straight blades with NACA0020 profile, solidity σ of 7%, and aspect ratio ($AR=H/D$, where H is the blade length) of 1.6; the reader can find details in Vergaerde *et al.* (2020). Figure 1 shows horizontal profiles of U/U_0 (where U is the streamwise velocity, and U_0 is the freestream velocity, equal to =10.7 m/s) achieved with CFD at various locations along x-axis (normalised by D) downstream the rotor axis; the z-coordinate corresponds to the blade midspan. In Fig. 1-a, the sensitivity of results to the number of revolutions is reported; it can be seen that for the near and medium wake (until $x/D=6$) it is sufficient to simulate 18 revolutions, whereas at $x/D=8$ the wake needs at least 21 revolutions to be considered completely developed. A sufficient agreement has been found by the comparison between the CFD results (achieved after 18 revs.) and the experimental measurements, as shown in Fig. 1-b.
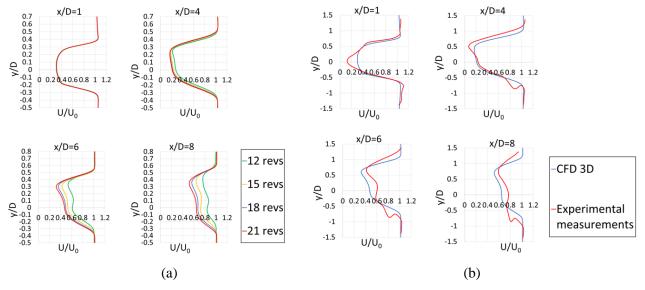

Figure 1: streamwise velocity profiles achieved by CFD at different x-locations: (a) effect of revolution number; (b) comparison with experimental data from Vergaerde *et al.* (2020).

2.2   Momentum budget approach

To find the physical mechanisms that mostly favor the wake recovery, the streamwise Reynolds Averaged Navier-Stokes (RANS) momentum equation is rearranged as in Bachant and Wosnik (2015) and Ouro *et al.* (2019), assuming the steadiness and incompressible of the flow:

$$\frac{\partial \overline{U}}{\partial x} = -\frac{\overline{V}}{\overline{U}}\frac{\partial \overline{U}}{\partial y} - \frac{\overline{W}}{\overline{U}}\frac{\partial \overline{U}}{\partial z} - \frac{1}{\rho \cdot \overline{U}}\frac{\partial \overline{P}}{\partial x} - \frac{1}{\overline{U}}\frac{\partial}{\partial x}\overline{U'U'} - \frac{1}{\overline{U}}\frac{\partial}{\partial y}\overline{U'V'} - \frac{1}{\overline{U}}\frac{\partial}{\partial z}\overline{V'W'} + \frac{\nu}{\overline{U}}\left(\frac{\partial^2 \overline{U}}{\partial x^2} + \frac{\partial^2 \overline{U}}{\partial y^2} + \frac{\partial^2 \overline{U}}{\partial z^2}\right) \qquad (1)$$

The physical meaning of all terms on the right hand of Eq. (1) is specified in Table 1: lateral and vertical advection, streamwise pressure gradient, three terms of turbulent transport (x, y and z derivatives of the Reynolds stresses), viscous diffusion. All terms are normalized by D/U_0, and spatially averaged over cross-sections placed at various distances downstream the rotor, yet limiting the averaging operation to the wake portion contained within the iso-contour of velocity magnitude corresponding to U_0 as done by Posa (2020). The values of the contributions to streamwise momentum recovery were obtained using the time-average values of the flow field achieved during the last two turbine revolutions.

Table 1: Terms used to compute contributions to streamwise momentum recovery

y advection	$-\bar{V}/\bar{U} \cdot (\partial\bar{U}/\partial y)$
z advection	$-\bar{W}/\bar{U} \cdot (\partial\bar{U}/\partial z)$
pressure transport	$-(1/\rho \cdot \bar{U}) \cdot (\partial\bar{P}/\partial x)$
x turbulent transport	$-1/\bar{U} \cdot (\partial\overline{U'U'}/\partial x)$
y turbulent transport	$-1/\bar{U} \cdot (\partial\overline{U'V'}/\partial y)$
z turbulent transport	$-1/\bar{U} \cdot (\partial\overline{U'W'}/\partial z)$
viscous diffusion	$\nu/\bar{U} \cdot (\partial^2\bar{U}/\partial x^2 + \partial^2\bar{U}/\partial y^2 + \partial^2\bar{U}/\partial z^2)$

It should be observed that a first advantage of CFD is the possibility to calculate all the terms appearing in Eq. (1), whereas in experimental tests this would be technically difficult or very expensive. For instance, the contributions of the streamwise pressure gradient and the streamwise turbulent transport were not computed by Bachant and Wosnik (2015) and Ouro *et al.* (2019) due to the objective difficulty to obtain gradients; furthermore, in Bachant and Wosnik (2015) the contribution of streamwise derivative of the viscous stresses was not computed, while in Ouro *et al.* (2019) the viscous diffusion was considered negligible and then it was omitted. Another advantage of CFD is to be able to use very small computation cells, which leads to finer resolution than experimental work for the terms in Eq. (1). Our grid, in the wake region, starting from 2D downstream the turbine axis and up to the domain outlet, is made of regular parallelepiped cells with uniform spacing in the three directions equal to: 0.43*c*, 0.35c and 0.28*c* along *x*, *y* and *z* respectively. To make a comparison, the data were taken on cross-sectional planes with resolution of 0.71*c* along *y* and 0.93*c* along *z* in Bachant and Wosnik (2015), and 1.17*c* along *y* and 0.68*c* along *z* in Ouro *et al.* (2019).

3. RESULTS

The section begins with a paragraph focused on the vortices generated at the blade tips. It will be show that the tip vortex strength depends on blade angular position, hydrofoil profile and turbine solidity, and that the characteristics of the large-scale rotating structures occurring in the turbine wake are determined by those of the tip vortices. Afterwards, the wake momentum replenishment will be analyzed on cross-sectional planes set along the wake, first qualitatively by observing the flow field velocity, then quantitatively by calculating spatial averages for the terms appearing on the streamwise momentum budget equation.

3.1 Origin and evolution of the vortices at the blade tips

We investigated the wake behaviour of four hydrokinetic CFTs with three straight blades, having same diameter (D = 6m) and aspect ratio (AR = 2) but different solidity (σ = 6.34% and 15.9%) and blade profile ("camber-in" and "camber-out", as previously defined).
The domain dimensions can be considered "infinite" (i.e., without any wall effect) since they are large: 12*D* upstream and 24*D* downstream the rotor in streamwise direction (*x*-axis); 24*D* in crosswise and in vertical directions. To limit the cell number, half turbine is simulated. Doing this, the rotating and the fixed domains have about 9.5x10⁶ and 2.6x10⁶ hexahedral cells, respectively. In order to assume sufficiently stable the results at least at 6*D* downstream the turbine axis, 20 revolutions have been simulated. For further distances the wake is considered not completely developed and then the results are discarded. TSR slightly higher than the optimal ones, found by mean of preliminary 2d-CFD simulations, were adopted: 1.6 for high solidity, and 2.75 for low solidity. Before analysing the flow fields, some definitions should be recalled. Fig. 1-a indicates the origin of the blade angular position (θ), and the "upwind" and "downwind" paths. Moreover, it will be practical to name "windward side" and "leeward side" of the wake the sides behind the windward (θ=-90°÷90°) and the leeward (θ=90°÷270°) passage of the blade, respectively (Fig. 1-c).

Experimental literature demonstrated the presence of large-scale coherent structures in the CFT wakes (Bachant and Wosnik 2015; Rolin and Porté-Agel 2018; Ryan *et al.* 2016; Ouro *et al.* 2019). Araya *et al.* (2017) provided evidence of three typical regions: (a) near-wake, governed by periodic blade vortex shedding; (b) transitional wake, in which the shear-layer generated between the low-velocity wake and the freestream by-pass flow became unstable; and (c) far-wake, governed by bluff body-like wake oscillations. We focus on (a) in the current paragraph and, with further details, on (a) and (b) in the next paragraphs. Whereas, (c) is out of our field of observation, as it is limited to *6D*.

Three kind of vorticities are released by a CFT blade, two of which are *z*-directed and then also visible in 2d-CFD simulations. The first is the skin friction vorticity occurring inside the boundary layer surrounding a body immersed in a fluid in motion. The second is the dynamic stall periodic vorticity, and its intensity and release timing depend on TSR: at low TSR the flow separation is significant long before reaching the maximum attack angle, therefore the vortex is released during upwind; at TSR above the pick performance the flow is little separated and then a weak vortex is released only at the upwind end (i.e., when the suction and pressure sides of the blade reverse each other). However, it should be observed that these *z*-vorticities play a negligible role in the wake recovery dynamics, as proved by the fact that 2d-CFD wakes appear much longer and poorly re-energized than 3d-CFD wakes.

The third type of vorticity is related to tip vortices, a fluid dynamic loss that consists in flow circulation over the tip occurring at the ends of any streamlined body (wings, turbine blades) because of a pressure difference between the two sides of the body. Tip vortex intensity is strong where the pressure difference is high, i.e.: at *θ* corresponding to great incoming-flow velocity and attack angle, therefore during central upwind and, in a less extent, central downwind (Zanforlin and Deluca, 2018) This it means that where the torque is greater, the strongest tip vortices also occur. Just as the airfoil shape influences torque distribution, it also affects the strength of the tip vortices released at a certain *θ*. As shown in Fig. 1-b, in comparison to the camber-out blade, the camber-in blade generates lower torque during upwind and higher torque during downwind, as also found by Qin *et al.* (2012). Results of Fig. 1-b suggest that: camber-out profiles imply strong tip vortices but only in upwind, whereas camber-in generate significant tip vortices also in downwind; extended blade surfaces (high solidity) generate greater torque in upwind but are also expected to cause higher circulation flowrate over the tips, therefore stronger tip vortices (in upwind).
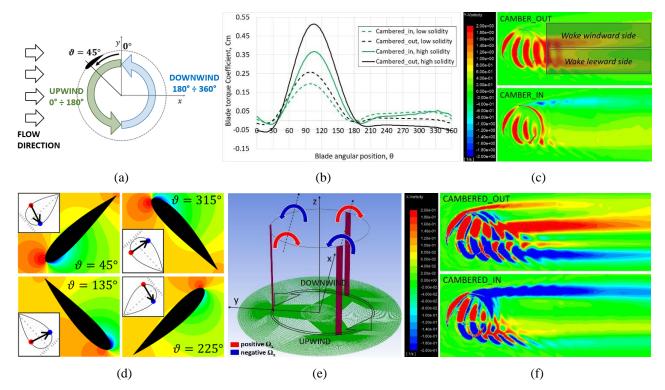

(a) (b) (c)

(d) (e) (f)

Figure 2: a) definitions of *θ*, upwind and downwind paths; b) blade instantaneous torque coefficient for the 4 turbines of interest; c) pressure maps for four *θ* values in case of the low *σ* and camber-in turbine; d) *y*-vorticity on a plane at *z*=H/2 for the low *σ* turbines; e) schematic of the *x*-rotation verse in each of the 4 quadrants; f) *x*-vorticity on a plane at *z*=H/2 for the low *σ* turbines.

5

Not only the intensity but also the spatial orientation of the rotation axis of tip vortices has important consequences on the large-scale motions in near wake. The major component of the tip vorticity is the y-component, that is depicted in Fig. 1-c on a horizontal plane located at the height of the blade tips (z=6m) for the low-σ turbines (here the blades are at $\theta = 0°$, 120° and 240°). It can be seen that y-vorticity is only positive, which is intuitive, and during upwind it is more intense for the camber-out profile than for the camber-in, as previously justified. The x-component is much smaller than the y (in our calculations it resulted from half to an order of magnitude lower) and its direction varies with the angular position of the blade. To understand the dependence of the rotation direction from θ, it is useful to divide the blade path into 4 quadrants (first and second half upwind, first and second half downwind) and analyse the static pressure field around the blade when this is in the middle of each quadrant, then at 45°, 135°, 225° and 315° (Fig. 1-d). We calculated the positions on the blade profile for the centre of the overpressures acting on the pressure-side and for the centre of the low pressures acting on the suction-side, then we joined the two centres with an arrow, as visible on the small figures in overlay. Since the flow passes over the blade driven by the pressure difference, it is plausible to assume that the direction of motion is roughly represented by the arrow. It follows that the sigh of the x-vorticity will be positive for the first half of upwind and downwind, and negative for the second half of upwind and downwind, as schematised in Fig.1 e). It is worth noting that the direction of the arrows differs little from that perpendicular to the blade chord, and that consequently the verse of the x-vorticity only depends on the quadrant, regardless of the airfoil type.

The vortices generated at the blade tips are advected downstream the turbine by the freestream, those generated in upwind will interact with those generated in downwind, the weakest will disappear because of viscosity (or will be disrupted by vortices with opposite rotation verse) while only the strongest will still be observable in the wake. Fig. 1-f) shows the x-vorticity on the horizontal plane at z=6m in case of the low solidity turbines. It can be observed that the strongest tip vortices generated during the blade rotation persist in the near-wake. They are, for camber-out blade: the positive vortices generated during the first half of upwind, on the wake windward side; the negative vortices generated during the second half of upwind, on the wake leeward side. For camber-in blade: the negative vortices generated in the second half of downwind, on the wake windward side; a mix of negative and positive vortices generated, respectively, in the second half of upwind and in the first half of downwind, on the wake leeward side. Finally, we point out that the aforementioned division of the blade path in four quadrants is a simplification since, to be more precise, the extension of the first quadrant is more than 90° as proved by the fact that in Fig. 2-f the x-vorticity released by the blade at θ=120° is still red, and this also implies that the second quadrant is much less wide than 90°.

3.2   Wake development and recovery: qualitative observations of the flow field

The effect of the blade profile on the wake recovery is impressively exemplified in Fig. 3, depicting the time-averaged velocity vectors projected on the vertical plane y=0 (i.e., the plane passing through the turbine axis) for the high solidity turbines. Yellow lines indicate the x-positions corresponding to 1D, 2.5D, 4D and 6D downstream the turbine axis. It can be seen that camber-out blades allow a much faster replenishment of the velocity deficit region than camber-in blades. Despite a single vertical view is not sufficient to capture the 3d features of the wake, this figure suggests the occurrence of very different mechanisms of momentum recovery that are attributable only to the blade shape, since this is the only difference between the two turbines.

To recognize these mechanisms, it is useful to analyse the wake evolution on transversal planes placed at 1D, 2.5D, 4D and 6D from the rotor axis as depicted in Figs. 3 and 4, respectively showing the cross-wise velocity vectors and the streamwise velocity maps that have been time-averaged over the last two revolutions. The overlay added rectangular frame indicates the frontal size of the (half, for symmetry) turbine, moreover is must be specified that the observer is located upstream the turbine, therefore the windward side of the wake is on the left and the leeward side is on the right. We define "wake" the region characterised by a velocity deficit respect to U_0, therefore the region coloured by blue, green and yellow. U_0 corresponds to the orange, whereas the red region surrounding the wake indicates the high-momentum by-pass freestream which presence is crucial for the gradual replenishment of the wake streamwise momentum.

Let's start with the high solidity case and camber-out blades: a pair of counter-rotating vortices is visible at x=1D; the rotation verse of each vortex is the same observed in Fig. 2-e and 2-f, and it is coherent with the tip vortices generated during the upwind passage of the blades; the rotation verses are such as to induce a massive vertical advection which reintroduces momentum into the top of the wake (visible at x=2.5D); since the vortex on the windward side of the wake is much larger and stronger than the one on the leeward side, the energy recovery is asymmetrical and mostly located at the upper-leeward corner of the wake. Similar features were

6

also found by Bachant and Wosnik (2015) and Rolin and Porté-Agel (2018) in case of symmetrical airfoils and solidities close to the ours. Furthermore, it can be noted that the small vortex on the right is rapidly dissipated and supplanted by the left vortex which, although progressively weakened, continues to widen exerting a momentum reintroduction action also on the leeward side of the wake (where lateral advection is "positive"). However, the mechanisms generated by the dominant vortex involve not only re-energizing the wake but also, on the contrary, extending the velocity deficit on the wake windward side where the flow moves out of the wake ("negative" lateral advection) because of the rotation verse of the vortex. As a result, at 4D and 6D the residual velocity deficit, and therefore the wake, appear extensively shifted on the windward side while the wake leeward side and most of the region behind the turbine appear completely re-energized.
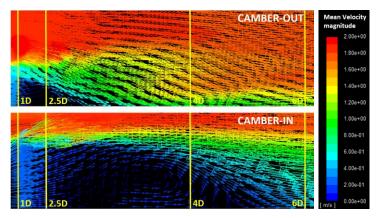

Figure 3: Time-averaged velocity vectors on the vertical plane *y*=0 for the high solidity camber-out (top) and camber-in (bottom) turbines; yellow lines indicate some *x*-positions downstream the turbine axis.
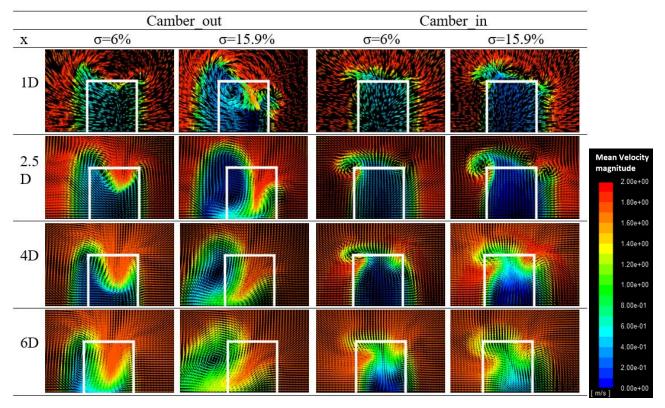

Figure 4: Time-averaged cross-wise velocity vectors on transversal planes at 1*D*, 2.5*D*, 4*D* and 6*D* downstream the turbine axis, for the four turbines (colormap based on velocity magnitude).

Fig. 4 shows a completely different wake evolution in case of high solidity camber-in blades. At 1*D* and 2.5*D* at the top of the wake a pair of small counter-rotating vortices can be seen, which origin is attributable to the tip vortices generated during downwind. A third small vortex is visible further to the right as a consequence of tip vortices generated in the second-half of upwind, as already revealed by fig. 2-f. These vortices are smaller

and much weaker than in case of camber-out profile so their momentum replenishment action is minor and only limited to the lateral advection visible at the wake windward side and to the upper-leeward corner, where freestream is entering into the wake. It should be observed that the rotation verse of the vortex pair generated during downwind implies "negative" vertical advection (i.e., the flow is outgoing the wake). Moreover, "negative" lateral advection is observable at the wake leeward side, coherently with the rotation verse of tip vortices generated during the second half of upwind, and, as a result, the wake appears slightly deviated on the right. Unlike the case of camber-out profile, these vortices are dissipated very quickly, so much so that further downstream than 2.5D no trace of them is seen anymore. Most of the recovery process takes place further ahead, at 4D and 6D, where flows entering the wake can be seen from all directions; however, these motions instead to being correlated to tip vortices are due to the natural collapse of the wake as it is characterized by lower pressure than the high momentum flow that surrounds it. Comparing the streamwise velocity deficit at 6D for the cases with camber-out and camber-in profiles (Fig. 5) it is evident that the latter entail a much slower wake recovery. One last detail is worth observing, regarding the occurrence of negative streamwise velocities in the wake centre in case of camber-in profile and high solidity. This is due to the wide recirculating region visible in Fig. 3. Negative streamwise velocities in CFT wakes were also noticed in experimental studies (Araya *et al.* 2017; Brownstein *et al.*, 2019; Parker and Leftwich 2016; Rolin and Porté-Agel 2015) and in other numerical works (Chatelain *et al.* 2017; Hezaveh *et al.* 2017).

In case of low solidity, the wake evolution for camber-out and camber-in blades is qualitatively similar to the respective high solidity cases, as depicted in Figs. 4 and 5, but the momentum recovery is slower and less complete. Indeed, at 6D it can be seen that the residual deficit of momentum is greater for both the low solidity turbines in comparison to the high solidity ones. The reason could be smaller intensity of blade tip vortices.
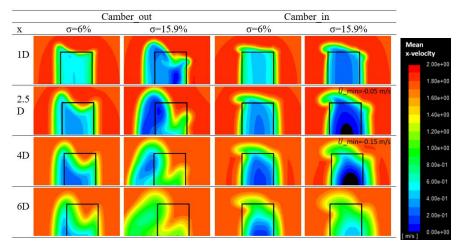

Figure 5: Time-averaged streamwise velocity on transversal planes at 1D, 2.5D, 4D and 6D downstream the turbine axis, for the four turbines.

3.3 Wake development and recovery: momentum budget computations

On the right hand of Eq. (1) there is the gradient of the streamwise velocity along *x*-axis, then a positive value means that the *x*-momentum is recovering while a negative value means that it is decreasing further. A positive value for a term on the right hand means that it is contributing to the wake recovery, for instance, a positive *y*-advection (or lateral advection) indicates that flow moving along the *y*-axis is (on average) entering the wake. Let's see how the terms on the right side which we have not yet discussed appear on transversal planes placed at 2.5D, 4D and 6D. Fig. 6 shows the pressure transport term, calculated as described in section 2.2. Negative values (blue on the maps) for this term mean that the pressure is increasing and therefore prevents the *x*-momentum recovery. As can be seen, regardless of the blade shape and solidity, the prevailing color inside the wake is blue since the wake is characterized by low velocity and pressure and, moving away from the turbine, both the velocity and the pressure increase tending towards their freestream values. Although no comparisons can be found in literature as no one has shown the behavior of this term in fully 3d studies, it is expected that in general this term does not give a positive contribution to the wake recovery. In Fig. 6 a sudden change of color (from blue to red) is visible at 2.5D and 4D for the high solidity with camber-in blades. Its appearance seems devoid of physical meaning and solely attributable to the negative values of *x*-velocity already noticed in Fig. 3. in the wake core. In fact, all terms on the right side of Eq. (1) are divided by the local x-velocity, then

this event can be considered a formulation defect, which needs to be corrected in the future. Figs. 7 and 8 show the *y* and *z* turbulent transport terms. In accordance with the literature (Rolin and Porté-Agel 2018), the prevailing color is red (i.e, positive contribution to the recovery) and the zones with the highest values are localized where strong velocity gradients occur, therefore at the boundaries of the wake (and, in case of camber-in profile, in the core). Another aspect in line with the theory is that the turbulent mixing is a relatively "late" phenomenon, in that it is significant starting from the medium wake (see that at 4*D* it is higher than at 2.5*D*). It is also interesting to note that high solidity implies much greater turbulent transport than low solidity and therefore higher aptitude to the wake recovery. In case of high solidity and camber-in profile, unrealistic blue spots are visible inside the wake where the *x*-velocity is negative, this means that if we correct the formulation we would get even higher values for turbulent transport.
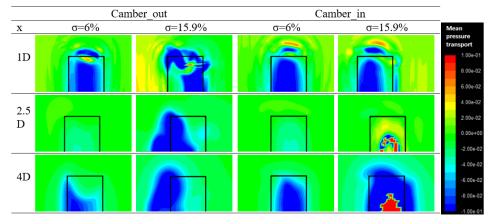

Figure 6: Time-averaged values of the pressure transport on transversal planes at 1*D*, 2.5*D*, 4*D* and 6*D* downstream the turbine axis, for the four turbines.
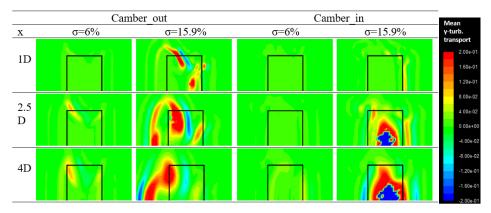

Figure 7: Time-averaged values of the *y*-component of the turbulent transport on transversal planes at 1*D*, 2.5*D*, 4*D* and 6*D* downstream the turbine axis, for the four turbines.
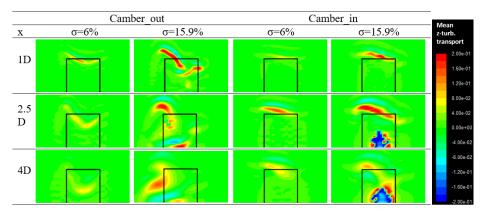

Figure 8: Time-averaged values of the *z*-component of the turbulent transport on transversal planes at 1*D*, 2.5*D*, 4*D* and 6*D* downstream the turbine axis, for the four turbines.

The diagrams in Fig. 9 report the streamwise evolution for all the terms at the right hand of Eq. 1, and for their sum (i.e., the term at the left hand). We can observe that: for camber-out profile, z-advection is positive already starting from the near-wake, while for camber-in profile both the advection terms are negative in the near-wake and became positive later, when the wake collapse; the turbulent transport terms are important only in case of high solidity, and they give an important contribution to the momentum recovery at $3.5D$ for camber-out profile and at $4.5D$ for camber-in profile; the viscous diffusion term is negligible for all the cases. It is not surprising that, in case of high solidity and camber-out profile, after $3D$ y-advection seems to exceed z-advection, in fact this happens as the main flow entering the wake becomes oblique, that is, it has both z and y components, as clearly visible in Fig. 4 at $4D$ and $6D$.
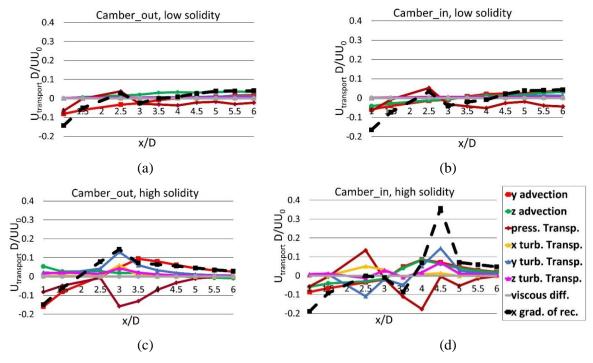

Figure 9: Streamwise evolution of the non-dimensional cross-stream averages of all terms in Eq. (1) for: a) σ=6% camber_out; b) σ=6% camber_in; c) σ=15.9% camber_out; d) σ=15.9% camber_in.
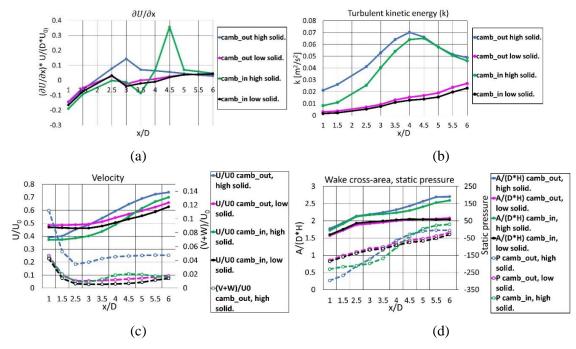

Figure 10: Evolution of the cross-stream averages of: a) gradient of the streamwise velocity recovery; b) turbulent kinetic energy; c) U and crosswise velocity; d) static pressure and wake cross-sectional area.

The left-hand side of Eq. 1 is compared for the four turbines in Fig. 10-a: wake recovery appears delayed for camber-in profile; low solidity implies slower recovery for both the profiles. Fig. 10-b indicates a remarkable occurrence of turbulent kinetic energy in case of high solidity, especially from the medium-wake. Fig. 10-c shows the streamwise velocity and the modulus of the cross-wise velocity, the latter being higher in case of high solidity, especially for camber-out profile due to the main vortex that persists long far in the wake. Fig. 10-d shows the pressure recovery, that is faster for high solidity, and the wake cross-wise area, that is larger and continuously increasing in case of high solidity, while an asymptote is reached from $3D$ for low solidity. Given these results, and considering the interesting potential in terms of high starting torque (Rainbird *et al.* 2015), especially if a variable pitch is adopted (Kirke and Lazauskas 1991), we can conclude that camber-out profiles could be the most suitable choice also for farms thanks to their wake recovery properties.

4. CONCLUSIONS

Blade tip vortices can be considered the main precursors of the large-scale flow structures found in the wake of CFTs. The main findings of our analysis on the origin and characteristics of tip vortices and on the wake recovery mechanisms, in relation to the turbine geometry, are:
- Since the strength of the blade tip vortices depends on the pressure difference between the two sides of the blade, it is very high during upwind for camber-out profiles while it is more smoothly distributed between upwind and downwind for camber-in profiles.
- The x-vorticity of the blade tip vortices determines the rotation verse of the vortices in the wake; since its sign only depends on the revolution quadrant, the sign of the wake vortices is established by the quadrants where strong tip vortices are generated.
- A pair of counter-rotating vortices occurs in the wake at the turbine top and bottom ends, which rotation verse depends on blade profile and it is such as to generate positive vertical advection for camber-out profiles, but negative vertical advection for camber-in profiles.
- The blade tip vortices of camber-out profiles are very effective in supporting wake recovery, being the vertical advection induced by tip vortices the main contribution to the momentum recovery.
- For camber-in profiles the strength of tip vortices is too small and their rotation verse is poorly effective to support the momentum recovery, that appears delayed and mainly governed by wake collapse and turbulent transport.
- Higher solidity implies much stronger tip vortices and therefore faster wake recovery.
- For both the profiles, turbulent transport is significant in case of high solidity.

REFERENCES

Araya, D.B., Colonius, T., Dabiri, J.O. (2017) Transition to bluff-body dynamics in the wake of vertical-axis wind turbines. *J. Fluid Mech.*, **813**:346-381.

Bachant, P., Wosnik, M. (2015) Characterising the near-wake of a cross-flow turbine. *Journal of Turbulence* **16**(4):392-410.

Balduzzi, F., Bianchini, A., Maleci, R., Ferrara, G., Ferrari, L. (2016) Critical issues in the CFD simulation of Darrieus wind turbines. *Renew. Energy* **85**:419–435.

Brownstein, I.D., Wei, N.J, Dabiri, J.O. (2019) Aerodynamically Interacting Vertical-AxisWind Turbines: Performance Enhancement and Three-Dimensional Flow. *Energies* **12**: 2724.

Chatelain, P., Duponcheel, M., Zeoli, S., Buffin, S., Caprace, D-G., Winckelmans, G., Bricteux, L. (2017) Investigation of the effect of inflow turbulence on vertical axis wind turbine wakes. *IOP Conf. Series: Journal of Physics: Conf. Series* **854**:012011.

Dabiri, J.O. (2011) Potential order-of-magnitude enhancement of wind farm power density via counter-rotating vertical-axis wind turbine arrays. *J Renew Sustain Energy* **3**:43104.

Hezaveh, S.H., Bou-Zeid, E., Lohry, M.W., Martinelli, L. (2017) Simulation and wake analysis of a single

vertical axis wind turbine. *Wind Energy* **20**(4):713-730.

Kinzel, M., Mulligan, Q., Dabiri, J.O. (2012) Energy exchange in an array of vertical-axis wind turbines. *Journal of Turbulence*, **13**:1-13.

Kirke, B.K., Lazauskas, L. (1991) Enhancing the Performance of Vertical Axis Wind Turbine Using a Simple Variable Pitch System. *Wind Engineering* **15**(4):187-195.

Maître, T., Amet, E., Pellone, C. (2013) Modeling of the flow in a Darrieus water turbine: Wall grid refinement analysis and comparison with experiments. *Renew. Energy* **51**:497–512

Menter, F.R. (1994) Two-equation eddy-viscosity turbulence models for engineering applications. *AIAA J.* **32**:1598–1605.

Ouro, P., Runge, S., Luo, Q., Stoesser, T. (2019) Three-dimensionality of the wake recovery behind a vertical axis turbine. *Renewable Energy* **133**:1066-1077.

Parker, C.M., Leftwich, M.C. (2016) The effect of tip speed ratio on a vertical axis wind turbine at high Reynolds numbers. *Experiments in Fluids* **57**(5):74.

Posa, A. (2020) Dependence of the wake recovery downstream of a Vertical Axis Wind Turbine on its dynamic solidity. *J. Wind Engin. & Industrial Aerodyn.* **202**:104212.

Qin, N., Danao, L.A., Howell, R. (2012) A numerical study of blade thickness and camber effects on vertical axis wind turbines. *Proceedings of the Institution of Mechanical Engineers Part A Journal of Power and Energy* **226**(7): 867-881.

Rainbird, J.M., Bianchini, A., Balduzzi, F., Peiró, J., Graham, J.M.R., Ferrara, G., Ferrari, L. (2015) On the influence of virtual camber effect on airfoil polars for use in simulations of Darrieus wind turbines. Energy Conversion and Management **106**:373-384.

Ryan, K.J., Coletti, F., Elkins, C.J., Dabiri, J.O., Eaton, J.K. (2016) Three-dimensional flow field around and downstream of a subscale model rotating vertical axis wind turbine. *Exp Fluids* **57**:38.

Rolin, V., Porté-Agel, F. (2015) Wind-tunnel study of the wake behind a vertical axis wind turbine in a boundary layer flow using stereoscopic particle image velocimetry. *J. Phys. Conf. Ser.* **625**, 012012.

Rolin, V.F.-C., Porté-Agel, F. (2018) Experimental investigation of vertical-axis wind-turbine wakes in boundary layer flow. *Renewable Energy* **118**:1-13.

Vergaerde, A., De Troyer, T., Muggiasca, S., Bayati, I., Belloli, M., Kluczewska-Bordier, J., Parneix, N., Silvert, S., Runacres, M.C. (2020) Experimental characterisation of the wake behind paired vertical-axis wind turbines, *J. Wind Engin. & Industrial Aerodyn.* **206**:104353.

Wilcox, D.C. Formulation of the k-ω turbulence model revisited. *AIAA J.* (2008) **46**:2823–2838.

Zanforlin, S., Nishino, (2016) T. Fluid dynamic mechanisms of enhanced power generation by closely spaced vertical axis wind turbines. *Renew Energy* **99**:1213-1226.

Zanforlin, S. (2018) Advantages of vertical axis tidal turbines set in close proximity: A comparative CFD investigation in the English Channel, *Ocean Engineering* **156**:358-372.

Zanforlin, S., Deluca, S. (2018) Effects of the Reynolds number and the tip losses on the optimal aspect ratio of straight-bladed Vertical Axis Wind Turbines. *Energy* **148**:179-195.